

High-harmonic spectroscopy of the nonadiabatic coupling via Floquet-Bloch states

Cong Zhao^{1*}, Lucie Jurkovičová^{2,3}, Xiaozhou Zou¹, Benjamin T. Q. Miller¹, Robert M. Jones¹, Martin Albrecht^{2,3}, Ondřej Finke^{2,3}, Jaroslav Nejd^{2,3}, Margarita Khokhlova¹, Ondřej Hort², Fabrice Catoire^{4*}, and Amelle Zair^{1*}

¹Attosecond Quantum Physics Laboratory, King's College London, Strand, London, WC2R 2LS, United Kingdom

²ELI Beamlines Centre, ELI ERIC, Za Radnicí 835, 252 41 Dolní Břežany, Czechia

³Czech Technical University in Prague, FNSPE, Břehová 7, 115 19 Prague 1, Czechia

⁴CELIA, CNRS-CEA-Université de Bordeaux, 351 Cours de la Libération, Talence, F-33405, France

*cong.zhao@kcl.ac.uk; fabrice.catoire@u-bordeaux.fr; amelle.zair@kcl.ac.uk

8 July 2025

Strong laser light drives complex quantum electron dynamics in solids, which is captured by the high-harmonic generation (HHG) process. Here we report the observation of laser-dressed Floquet-Bloch states (FBSs) at the edge of the Brillouin zone (BZ) in HHG, by driving a large-bandgap MgO crystal in the strong-field regime where the laser pulse is intense enough both to accelerate electrons to the BZ edge as well as to dress the bands. We experimentally show and numerically confirm that the HHG spectrum encodes the nonadiabatic coupling between the conduction bands and FBSs, induced by the high-intensity driver, when some high harmonics are resonant with the dressed band structure. This enables us to trace the bandgap morphology — expanding HHG-spectroscopy techniques to cover the HHG tomography of the BZ edge.

The ultrafast dynamics of electrons driven by intense light in solid-state systems have not been accessible until recent advances in strong-field physics and attosecond science [1–5]. High-harmonic generation (HHG), a workhorse of attophysics, has established itself as one of the most significant nonlinear phenomena arising from laser-matter interactions in the strong-field regime [6–12]. In the past few decades, this field of research has been extended from atomic and molecular targets to solids, with HHG first observed in large-bandgap materials [13, 14], promising a source of bright attosecond vacuum ultraviolet (VUV) pulses [4, 15, 16].

The microscopic mechanism of HHG in solids is understood within the framework of interband polarisation and intraband current [17, 18]. The interband polarisation in solid HHG involves (i) electron-hole pair generation induced by the strong field, (ii) acceleration within the bands, and (iii) recombination [19] (see the left-hand side of Fig. 1a), analogous to the semiclassical three-step model in gases. The intraband current comes from the Bloch oscillations of the electron in both the valence band (VB) and conduction band (CB), associated with the electron acceleration [19, 20]. The intraband current can also be interpreted as a quantum jump between the Wannier states, which has a Stark-shifted energy equal to the harmonic order [21]. Unlike HHG in gas targets, the excited electron wavepacket is not free but is constrained by the crystal band structure, enabling the electron to explore the shape of the band manifolds [22–25]. Thus, the HHG emission from solids holds the potential not only as VUV, light but also as an ideal tool for probing essential characteristics of solids such as the optical band dispersion [19, 26, 27], the crystal symmetry [24, 28, 29], the topological phase character [30, 31], and the electron correlations in materials [32–35].

In solids there is a natural spatial periodicity governed by the structure of the crystal, described by the Bloch states [36], where the electronic wavefunctions exhibit and inherit the

spatial properties of the lattice. In conventional nonlinear optics, solids interact with perturbative temporally periodic laser light — this introduces periodicity simultaneously in time and in space, giving rise to laser-dressed quasienergy states, known as the Floquet-Bloch states (FBSs) [37–41]. FBSs describe how an initial Bloch state splits into multiple replicas in a time-periodic field [42–45]. Such states have been successfully observed in some topological insulators at the Dirac point using angle-resolved photoemission spectroscopy (ARPES) [46, 47].

Although FBSs have been successfully and ubiquitously investigated within conventional perturbative optics, in the strong-field regime the contribution of FBSs to HHG in solids has been demonstrated only in theoretical calculations [48–50]. In particular, FBSs were predicted to modify solid-HHG emission by altering selection rules, which cannot be fully explained by existing conservation laws [28]. Moreover, the interplay between FBSs and the intrinsic solid-state band structure has not been comprehensively explored, including in the momentum region near the edge of the Brillouin zone (BZ), where CBs either approach or cross each other.

Near the edge of the BZ the energy gaps between the first few CBs are usually less than one photon energy of the driving field, leading to complex dynamics involving several CBs. For high-intensity drivers, this region is reached when the amplitude of the electron excursion in the momentum space becomes comparable to the reciprocal of the crystal spatial periodicity a . This condition corresponds to the Bloch frequency $\omega_B = E_0 a$ in the laser field with strength E_0 being comparable to the frequency of the laser ω_0 , or $\omega_B/\omega_0 \approx 1$, where ω_B/ω_0 is a parameter [51] analogous to the Keldysh parameter for the gas phase and allows us to describe the equivalent of a strongly-driven regime. As the FBSs are modulated and separated by the laser photon energy $\hbar\omega_0$, the FBSs and the first few CBs inevitably intersect at the BZ edge, leading to the nonadiabatic coupling between these states. This com-

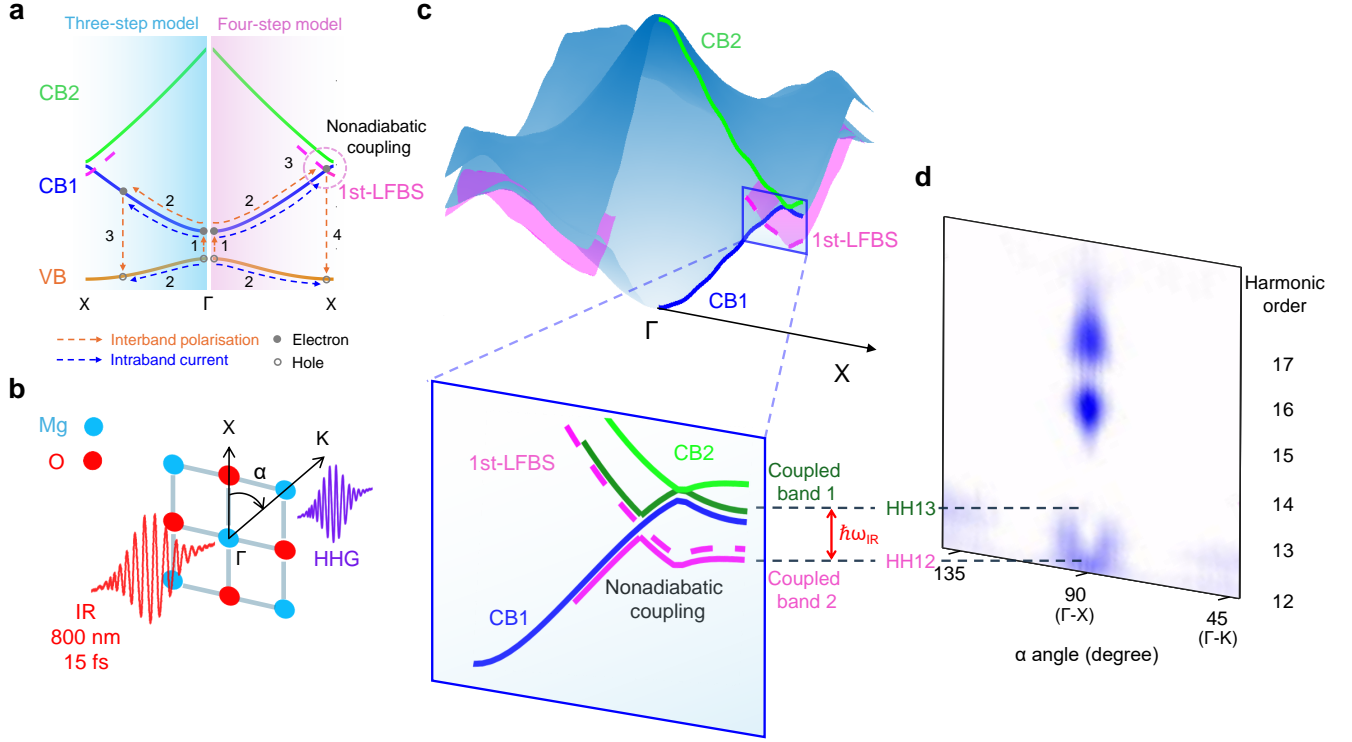


Figure 1 | Nonadiabatic coupling of the dressed-band structure in solid HHG. **a** Left: Three-step model for HHG in solids; Right: Four-step model for HHG in solids, when laser frequency is comparable to the Bloch frequency. **b** Schematics of the experiment: IR laser pulse with driving frequency 800 nm, peak intensity 3.6×10^{13} W/cm² and duration 15 fs (full width at half maximum, FWHM, in intensity), is incident perpendicular on the (100) surface of MgO; Γ -X and Γ -K directions correspond to Mg-O and Mg-Mg lattice directions; HHG signal (purple) is measured in transmission geometry, so it is collected from the backside of the crystal. **c** Band structure plot illustrating the nonadiabatic coupling between the 1st-LFBS and CB1, leading to the appearance of the reshaped coupled bands. **d** Measured HHG spectrum as a function of crystal orientation angle. The HH12 and HH13 encode information about the nonadiabatic coupling process, which exhibits a unique arc-like structure around the Γ -X direction.

plex phenomenon includes contributions from multiple physical processes, such as multiband dynamics, nonadiabatic coupling, and laser-induced Floquet states. Although recent studies have introduced quantum-optical scenarios in the HHG process beyond the semiclassical picture [52], such as light-induced phase transitions [34, 53, 54] and Landau-Dykhne-type transitions [55], the nonadiabatic coupling that involves FBSs under the strong-field regime has never been observed or measured.

In this work we apply HHG spectroscopy to investigate the nonadiabatic coupling at the BZ edge in the strong-field regime. We observe that the strong laser pulse induces nonadiabatic coupling between CBs and their FBSs, with FBSs being observed for the first time to our knowledge, in the strong-field regime in a large-bandgap magnesium oxide (MgO) monocrystal (see Fig. 1b). The emitted high-order harmonics (HH) serve as an effective probe in strongly-driven regime, allowing access to the region near the BZ edge, where the complex behaviour of the band structure is typically present. We analyse the scan of the HHG spectrum over the orientation of the crystal shown in Fig. 1d, which imprints the momentum space near the edge of the BZ, including the induced nonadiabatic coupling of the CBs and FBSs (see Fig. 1c). We examine the nonadiabatic coupling mechanism theoretically focusing on the interband process responsible for the 12th and 13th HH (HH12 and HH13) emission in MgO, where HHG signals are enhanced through nonadiabatic coupling. We confirm by numerically solving the time-dependent Schrödinger equation

(TDSE) the nonadiabatic coupling of FBSs with CBs near the BZ edge to HHG in solids [48, 56], and show how the energy differences between dressed CBs and the VB (bandgaps) are encoded in the HHG spectrum. This work reveals the four-step HHG mechanism, similar to the resonant HHG in gas media [57], where after (i) the laser-assisted excitation of the electron from the VB to a CB and (ii) its acceleration within the CB towards the edge of the BZ in the strongly-driven regime, (iii) the electron experiences and encodes the complex band structure, including nonadiabatic coupling of laser-dressed bands (analogously to a structured continuum, an autoionising state, for the gas HHG), (iv) followed by the recombination to the VB with emission of light (see the right-hand side of Fig. 1a). Our study underscores the critical role of the FBSs and the nonadiabatic coupling dynamics in the interband HHG process in solids in the strongly-driven regime.

Strong-field nonadiabatic coupling

In our experiment, we shine an intense infrared (IR) pulse on the large-bandgap MgO crystal and measure the transmitted HHG spectra, as shown in Fig. 1b. The high peak intensity of the driver allows the electron wavepacket to reach both the first and the second CBs (CB1 and CB2). Two CBs approach each other towards the edge of the BZ as illustrated in Fig. 1c, where along the Γ -X direction, CB1 (blue curve) and CB2 (green curve) are separated by less than one photon energy of the IR driver. The periodicity of the laser field results in the appearance of Floquet replicas of CBs leading to

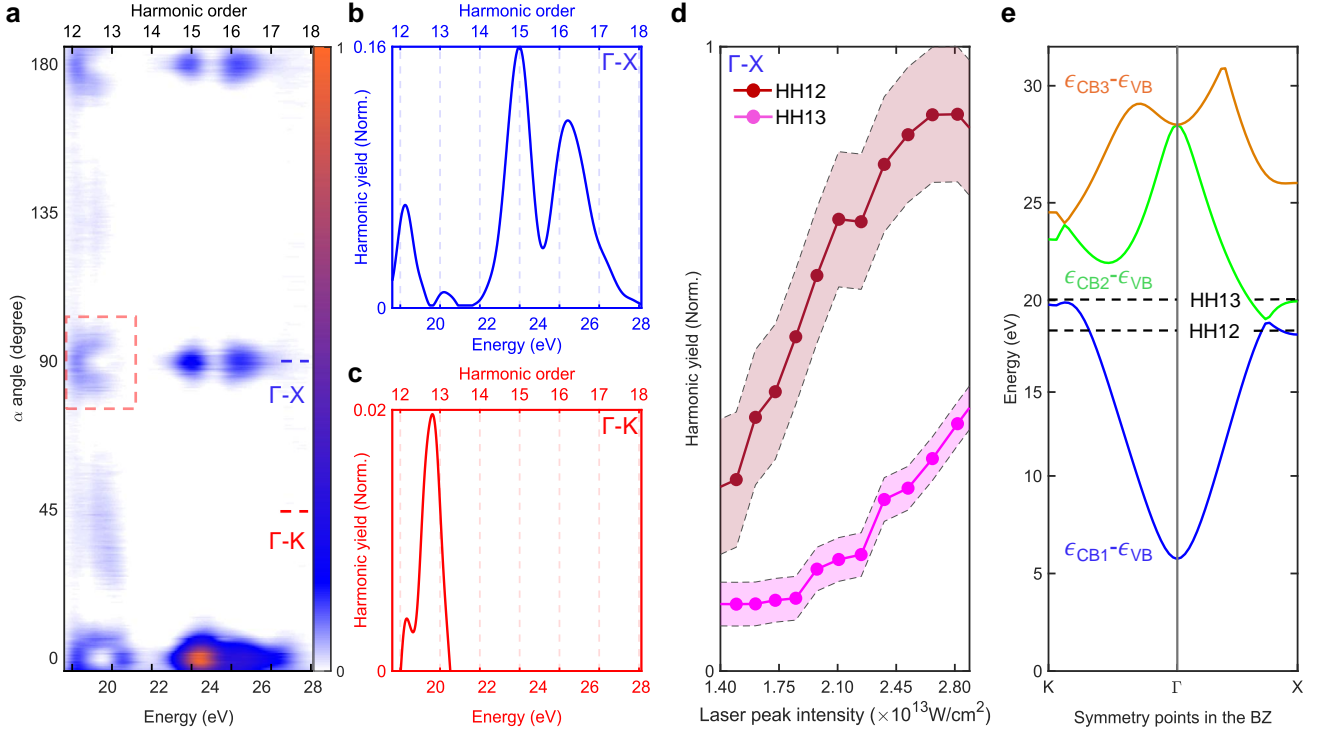


Figure 2 | Experimental results for HHG in MgO. **a** Orientation scan, defined by the azimuthal angle α , of the HHG spectrum normalised to the maximum intensity of HH15 at $\alpha = 0^\circ$; dashed rectangular shape defines the area of interest around 18-20 eV with the arc-like distribution of HH12 around the Γ -X direction. **b,c** HHG spectra at **(b)** $\alpha = 90^\circ$ (Γ -X) showing the presence of multiple harmonic orders, and **(c)** $\alpha = 45^\circ$ (Γ -K) showing single odd HH13, while HH12 appears at both angles. **d** Total HHG yield of HH12 and HH13, integrated over the full HH linewidth, as a function of laser peak intensity in Γ -X direction. **e** Bandgap structure of MgO in Γ -X (right) and Γ -K (left) directions showing a near-closing of the gap between CB1 and CB2 at the BZ edge around the two directions.

the emergence of the first-order lower FBS (1st-LFBS, purple dotted curve) of CB2, lying one photon energy below CB2 and intersecting with CB1, as shown in Fig. 1c in the zoom. At this crossing point the nonadiabatic coupling between the two states inevitably occurs.

This nonadiabatic coupling is described by the interaction Hamiltonian for two states

$$H_{\text{couple}} = \begin{pmatrix} \epsilon_{\text{CB2}} - \hbar\omega_{\text{IR}} & V \\ V^\dagger & \epsilon_{\text{CB1}} \end{pmatrix}, \quad (1)$$

where ϵ_{CB1} and ϵ_{CB2} are the eigenenergies of CB1 and CB2, $\epsilon_{\text{CB2}} - \hbar\omega_{\text{IR}}$ refers to the 1st-LFBS of CB2, and $V = \langle \text{CB1} | \mathbf{A} \cdot \mathbf{p} | \text{CB2} \rangle$ with $|\text{CB1}\rangle$ and $|\text{CB2}\rangle$ denoting the two eigenstates (typically obtained from density functional theory (DFT) calculations, see Methods). Diagonalising the Hamiltonian (1), we obtain the coupled band 1 (dark green curve) and coupled band 2 (purple curve), as shown in Fig. 1b.

Experimental results

We explore in detail the orientation scan over the azimuthal angle α of the HHG spectrum in MgO, shown in Fig. 2a. We focus on the energy range around the second plateau of the spectrum [29, 55, 58] in the energy region between 18 eV and 28 eV, where multiple CBs contribute significantly to HHG near the BZ edge.

First, we look at the main directions defined by the MgO crystal symmetry. The orientation scan of the HHG spectra exhibits generally four-fold symmetry, where the HHG is generated primarily at azimuthal angles $\alpha = 90^\circ$ (Γ -X) and

$\alpha = 45^\circ$ (Γ -K) with a period 90° . Along the Γ -X (Mg-O) direction, Fig. 2b, odd HHs, including HH13 and HH15, are generated, as well as, unexpectedly, even HH12 and HH16, which are forbidden due to inversion symmetry, while along the Γ -K (Mg-Mg) direction, Fig. 2c, only HH13 is observed with an additional feature around HH12.

To understand the mechanism of the HH12 generation and its nontrivial orientation-dependent arc-like behaviour, we analyse the total yield dependence on the laser intensity in the Γ -X direction for HH12 compared to spectrally closest odd HH13 (see Fig. 2d). For HH13 the yield increases monotonically with the peak intensity, while it moves from the cutoff to the plateau region and further through the different plateaus as multiband effects play a role from $1.40 \times 10^{13} \text{ W/cm}^2$ [23]. HH12, in contrast, exhibits a pronounced increase in its yield with peak intensity, starting in the cutoff region at a higher intensity than HH13, which potentially indicates the emergence of the FBSs at play.

We analyse the bandgap structure of MgO shown in Fig. 2e calculated within DFT [59] (see Methods for more details). From the bandgap structure we observe that the HH13 energy is close to the bandgap energy $\epsilon_{\text{CB2}} - \epsilon_{\text{VB}}$ (green curve) for $\alpha = 90^\circ$ or in Γ -X direction. The HH12 energy is close to $\epsilon_{\text{CB1}} - \epsilon_{\text{VB}}$ (blue curve) for the same direction. Thus, in the laser field the dressed CB2 state bandgap $\epsilon_{\text{CB2}} - \epsilon_{\text{VB}} - \hbar\omega_{\text{IR}}$, indeed, nearly overlaps with the CB1 one, resulting in the nonadiabatic coupling between 1st-LFBS and CB1, which is encoded in the orientation scan of the HH12 yield.

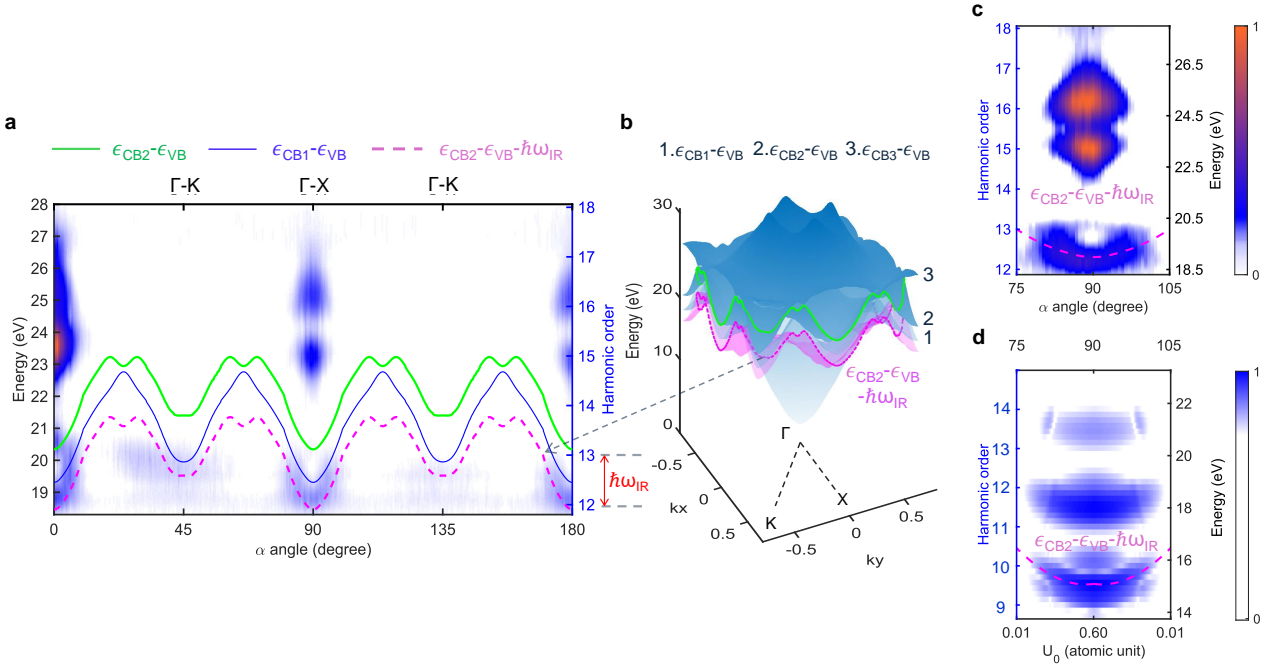


Figure 3 | Arc-like structure in the HHG spectrum orientation scan. **a** Comparison between the measured orientation scan of the HHG spectrum and theoretical bandgaps $\epsilon_{CB2} - \epsilon_{VB}$ (green solid curve), $\epsilon_{CB1} - \epsilon_{VB}$ (blue solid curve) and $\epsilon_{CB2} - \epsilon_{VB} - \hbar\omega_{IR}$ (purple dashed curve), extracted from panel (b). **b** 3D bandgap structure of MgO calculated within DFT (see Methods). **c** Fine experimental scan over orientation of HH12 spectra with an increment of 0.25° ; the purple dashed curve indicates the calculated bandgap value of $\epsilon_{CB2} - \epsilon_{VB} - \hbar\omega_{IR}$. **d** HHG spectra calculated as a TDSE solution for a 1D model potential, under the same laser conditions as for the experiment, where $U_0 = 0.6$ a.u. ($\epsilon_{CB2} - \epsilon_{CB1}$ is about 1 eV) mimics $\alpha = 90^\circ$ and $U_0 = 0.01$ a.u. (0.001 eV) mimics the case of $\alpha = 75^\circ$ and $\alpha = 105^\circ$. The calculated nonadiabatic coupling occurs in the energy range that covers HH9 and HH10 in 1D case (see Methods).

Arc-like fingerprint near BZ edge

To confirm our explanation of the arc-like structure in the orientation scan of the HHG spectrum through the nonadiabatic coupling of CB1 and 1st-LFBS, we compare the measured scan of the HHG spectrum with the orientation scan of the different MgO bandgaps calculated within DFT (see Methods) in Fig. 3a (also see 3D bandgap in Fig. 3b). One can notice that the 1st-LFBS of the CB2, shown with a dashed purple curve, matches the shape of the arc-like structure, as well as the CB1 bandgap has the same shape around Γ -X and Γ -K directions but is slightly shifted in energy. This matching suggests that the morphology of the second bandgap structure of MgO (CB2-VB) near the BZ edge shown in Fig. 3b is imprinted in the HH12 spectrum orientation scan, resulting in the arc-like structure.

Now we focus on the specific direction Γ -X, where the arc-like structure occurs most prominently. We analyse the fine orientation scan measured in this region shown in Fig. 3c along with our numerical 1D TDSE simulations shown in Fig. 3d, where the change in the model potential value U_0 mimics different crystal orientations (see Methods). In our simulation HH9 and HH10 qualitatively reproduce the behaviour of the experimental HH12 and HH13, with HH9 and the $\epsilon_{CB2} - \epsilon_{VB} - \hbar\omega_{IR}$ matching perfectly, which is consistent with the experimental results in Fig. 3c.

Nonadiabatic coupling at BZ edge

After numerically reproducing the arc-like structure in the experimental orientation scan of the HHG spectrum, we study in detail the nonadiabatic coupling causing this feature through the variation of the 1D model potential in the TDSE solution.

First, we concentrate on the very edge of BZ, $k = \pi/a$, and vary the potential depth U_0 , imitating a change in orientation, leading to a change in the bandgap between two CBs $\epsilon_{CB2} - \epsilon_{CB1}$ at the BZ edge, as well as to the change of energies of other bands and coupled bands. Figure 4a shows the behaviour of the bandgaps $\epsilon_{CB2} - \epsilon_{VB}$ (green curve) and $\epsilon_{CB1} - \epsilon_{VB}$ (blue curve) with the change of $\epsilon_{CB2} - \epsilon_{CB1}$, where $\epsilon_{CB1} - \epsilon_{VB}$ crosses the bandgap between the 1st-LFBS of CB2 and VB $\epsilon_{CB2} - \epsilon_{VB} - \hbar\omega_{IR}$ (green dashed curve) forming the nonadiabatic coupling of two states at $\epsilon_{CB2} - \epsilon_{CB1} \approx 1.8$ eV. As a result of the nonadiabatic coupling, two coupled bandgaps, shown in Fig. 4b with green (1) and purple (2) dashed lines, occur and form the forbidden crossing in the energy region corresponding to HH9 and HH10.

Now we analyse the behaviour of the calculated HHG spectrum at the edge of BZ while we change the parameters of the 1D potential, and therefore $\epsilon_{CB2} - \epsilon_{CB1}$ (see Fig. 4c-e). We calculate HHG spectra for 12.5 fs laser-pulse duration (Fig. 4c), which is close to the experimental one. We can see that both HH9 and HH10 encode the shape of the nonadiabatic coupling of 1st-LFBS of CB2 with CB1, repeating the superimposed dashed lines corresponding to Fig. 4b, which explains the initial arc-like structure in the HHG orientation scan.

To emphasise the structural shape of the curve in the HHG spectrum scan over $\epsilon_{CB2} - \epsilon_{CB1}$, we calculate the HHG spectrum behaviour for a longer laser pulse duration, 75 fs (see Fig. 4d), where harmonic lines are much narrower and well separated. In this case, HH9 and HH10 signals exhibit a stronger correlation with the coupled bandgap structures, showing clear resolution across the $\epsilon_{CB2} - \epsilon_{CB1}$ energy window, where the HH10 signal follows the shape of the coupled

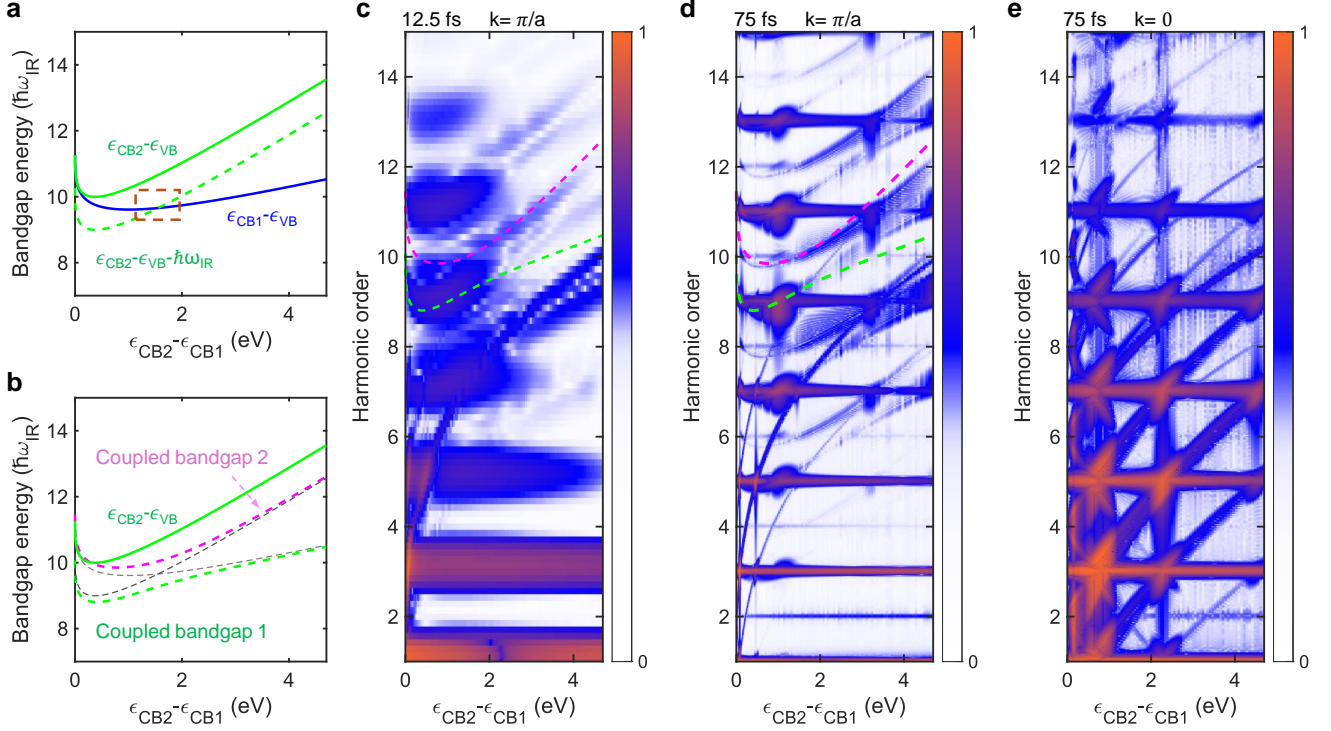


Figure 4 | TDSE simulations for HHG with varying 3D-adjusted 1D potential. **a** Bandgap from the 1D model potential as a function of $\epsilon_{CB2} - \epsilon_{CB1}$ at the BZ edge. The crossing of $\epsilon_{CB2} - \epsilon_{VB} - \hbar\omega_{IR}$ (green dashed curve) and $\epsilon_{CB1} - \epsilon_{VB}$ (blue solid curve) at ≈ 1.8 eV indicates the nonadiabatic coupling (orange dashed rectangle). **b** Coupled bandgap structure including the nonadiabatic coupling forming the coupled bandgap 1 (green dashed curve) and the coupled bandgap 2 (purple dotted curve) close to the energy of HH9 and HH10. **c-e** HHG spectra for laser pulse with duration (FWHM in intensity) (c) 12.5 fs at $k = \pi/a$ and (d,e) 75 fs at (d) $k = \pi/a$ and (e) $k = 0$.

band remarkably well. Thus, the calculated spectral curvatures of HH9 and HH10 capture the morphology of the coupled bandgap structures formed by the nonadiabatic coupling between the 1st-LFBS of CB2 and CB1. The mismatch between the coupled bandgaps and the two resonant harmonic spectra emerges when $\epsilon_{CB2} - \epsilon_{CB1}$ more than 2 eV, weakening the nonadiabatic coupling, which indicates that the process is more favourable to happen near the edge of the BZ, where the conduction bands are separated by less than one laser photon energy.

To confirm this idea, we compare HHG spectrum for the long laser pulse for the BZ edge $k = \pi/a$ and centre $k = 0$, shown respectively in Fig. 4d and e. A clear observation is that the coupled bandgap curvatures (green and purple dashed curves) are distinctly reproduced only for initial $k = \pi/a$ (d), and barely recognisable for $k = 0$ (e). This provides evidence that the main contribution to the nonadiabatic coupling in HHG in the large-bandgap solids originates from the edge of the BZ.

Conclusions

We investigate HHG from the large-bandgap MgO crystal in the strongly-driven high-intensity regime, close to the damage threshold, when the electron reaches the edge of the BZ. We observe harmonics HH12 in the Γ -X and Γ -K directions, which are forbidden due to the inversion symmetry. By scanning over the crystal orientation, we map the morphology of the bandgap near the BZ edge, which reveals a distinct arc-like fingerprint of HH12 in the orientation scan of the HHG spectrum. We show by numerically solving the 1D TDSE

that the behaviour of HH12 and HH13 is a result of the laser-dressing by the high-intensity laser field of the band structure, or occurrence of the FBSs, leading to the nonadiabatic coupling of the dressed bands near the edge of the BZ, where the bandgap between the first few conduction bands is smaller than one laser photon energy. This can be summarised in the four-step scenario of HHG where harmonics probe the complex nonadiabatically-coupled band structure near the edge of the BZ encoding it into the HHG orientation scan. Involving FBSs in HHG spectroscopy, we demonstrate how HHG spectroscopy can be expanded to access tomographic information in solids. Our approach opens a new route to dynamical and structural attosecond physics of condensed matter.

Methods

Material characteristics

In the experiment we utilise a *z*-cut MgO monocrystal (100 orientation) (United Crystal) of $1\text{ cm} \times 1\text{ cm}$ size as the target for HHG. The surface of MgO is two-sided, optically polished, and the thickness is measured to be $100\text{ }\mu\text{m}$. MgO crystallises in the rock-salt (NaCl) structure belonging to the cubic crystal system with the space group $Fm\bar{3}m$. Its unit cell is face-centred cubic (FCC) with a lattice parameter of approximately $a = 4.21\text{ }\text{\AA}$. The Mg-O bond length is about $2.1\text{ }\text{\AA}$, and the structure is highly symmetric with a density of approximately 3.58 g/cm^3 under standard conditions. The measured bandgap energy of MgO is about 7.8 eV .

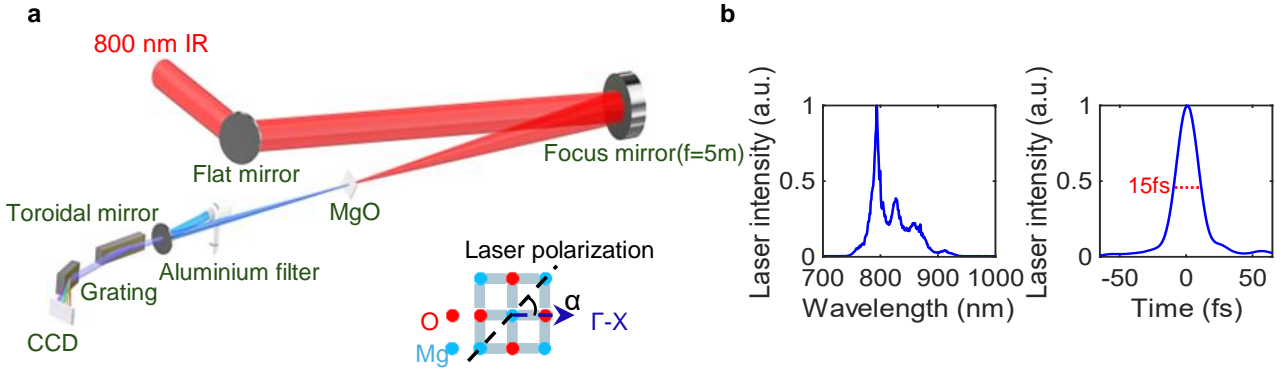


Figure 5 | **a** Schematic of the ELI-Beamlines setup with a broadband OPCPA driver used in the experiment. The laser beam is focused on a $100\ \mu\text{m}$ thick MgO monocrystal, cut along the (100) plane. A 3D motorised stage controls the crystal orientation with a step of 0.5° . **b** Measured spectral and temporal profiles of laser pulses.

Experimental setup

We measure HHG spectra generated in a $100\ \mu\text{m}$ MgO monocrystal, cut along the (100) plane. The experimental setup is shown in Fig. 5a, where the 15 fs less-than-6-cycle pulse is focused on MgO, using a spherical mirror with $f = 5\ \text{m}$. The HHG signal is filtered by a 150 nm aluminium foil and characterised by a calibrated XUV flat-field spectrometer with a CCD detector.

A 3D motorised stage is used to control the azimuthal crystal angle α over $[0 - 180]^\circ$ including the Γ -X (at 90°) and Γ -K (at 45°) directions, with an increment of 0.5° . The HHG signal is detected in a transmission configuration.

The laser, as shown in Fig. 5b, delivers infrared 15 fs pulses with 16.8 mJ energy at 1 kHz repetition rate by using a broadband optical parametric chirped-pulse amplification (OPCPA) system. 4% of the OPCPA energy is reflected by a wedge and used for HHG. The calculated laser peak intensity on target is $3.6 \times 10^{13}\ \text{W}/\text{cm}^2$, below the damage threshold of MgO that we measure to be $5.8 \times 10^{13}\ \text{W}/\text{cm}^2$, in agreement with [58].

In our experiment, interband HHG spectra are observed from the second plateau, in the energy window of 18–28 eV. In this energy range, HHG spectroscopy can probe the two first conduction bands CB1 and CB2, and the emergence of their FBSs, as well as the nonadiabatic coupling between them.

DFT calculation of band structure

The band structure of the bulk MgO crystal is calculated using DFT [59] approach. The Octopus package [60, 61] has been used for that purpose. The band structure is calculated using the adiabatic local-density approximation (LDA) [62] and employs SG15 norm-conserving pseudopotentials [63–65] (see Fig. 6).

It is important to note that within LDA, the bandgap of semiconductors and insulators is underestimated and does not account for excitonic effects. We used the scissor operator for better description the bandgap. Despite this discrepancy, the LDA approach correctly describes the dispersion of the VB and CBs thus properly describing the dynamics of intraband current and interband polarisation.

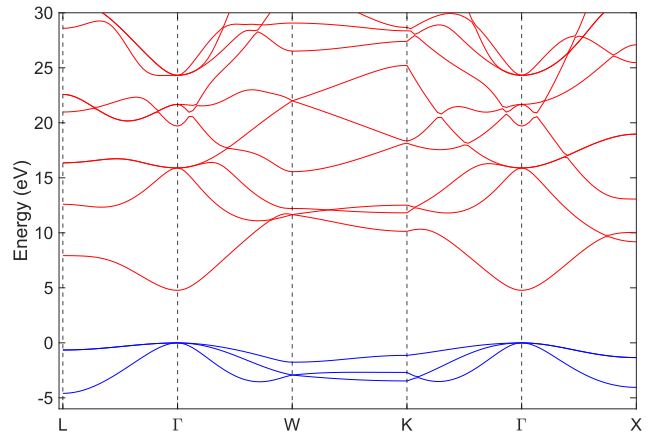


Figure 6 | MgO band structure calculated by DFT under LDA approximation. Red colour indicates CBs, while the blue colour refers to VBs.

TDSE calculation

We numerically solve TDSE with a 1D model potential $V(x)$, which follows the Kronig-Penney model. In this model, the potential well is centred at $x = 0$ and has a width of $a/2$ with $a = 8.2\ \text{\AA}$ being the periodicity of the system in the real space.

The wave function describing the system is given by the Bloch wave function $\Psi(x, t) = e^{ik_0x}u(k_0, x, t)$ with the reduced wave function $u(k_0, x, t)$, which is periodic in space with $2\pi/a$ periodicity, and the initial momentum k_0 . The reduced part of the Bloch wave function is obtained by solving the TDSE in the dipole approximation in the velocity gauge. The TDSE is explicitly given by

$$i\frac{\partial u}{\partial t} = \tilde{H}(k_0, t)u = \left\{ \frac{[P + k_0 + A(t)]^2}{2} + V(x) \right\} u, \quad (2)$$

where P is the electron momentum operator. $A(t)$ is the vector potential of the electromagnetic field, which has a central frequency ω_0 and an amplitude $A_0 = E_0/\omega_0$. Here $\omega_0 = 0.057\ \text{\AA}^{-1}$ (corresponding to wavelength 800 nm) and $E_0 = 0.007\ \text{\AA}^{-1}$. Using the velocity gauge ensures that we keep the periodicity of the Hamiltonian over time.

The wave function is decomposed on a plane wave basis and

is solved directly in real space. The propagation is performed using the Lanczos algorithm (with a basis of size 10) with the initial condition $u(k_0, x, t = 0) = \varphi(k_0, x)$. $\varphi(k_0, x)$ is the eigenstate of the stationary Schrödinger equation with eigenvalue $\epsilon_n(k_0)$, describing the band n . In this work, $\varphi(k_0, x)$ is the eigenstate for $n \geq 1$. Here we start with $n = 2$ to get the bandgap at the Γ point, same as for the DFT calculation. The numerical convergence is checked using the procedure of varying the grid parameters. Typically, 21 plane waves are used to fully converge the TDSE solution.

Once the wave function over time has been obtained, the HHG spectrum is calculated from the derivative of the current using the Ehrenfest theorem:

$$\frac{\partial J(k_0, t)}{\partial t} = \int dx u^*(k_0, x, t) \left[\frac{\partial V}{\partial x} + E(t) \right] u(k_0, x, t). \quad (3)$$

The total current is then found by integrating over k_0 in the BZ, that is

$$\frac{\partial J(t)}{\partial t} = \int_{BZ} dk_0 \frac{\partial J(k_0, t)}{\partial t}. \quad (4)$$

The power spectrum of the emitted harmonics is then evaluated by taking the Fourier transform of the current as

$$I_{\text{HHG}}(\omega) = \left| \omega \int_{-\infty}^{\infty} dt e^{i\omega t} J(t) \right|^2. \quad (5)$$

As mentioned above, the calculations are performed in the velocity gauge to ensure momentum conservation. In Eq. (1) of the main body of the article, the dressed-state picture is also performed using the velocity gauge (as the eigenvalues converge to the field-free states [66]) as can be seen from the matrix elements V . Note that for the particular case of the first-order nonadiabatic coupling there is gauge invariance of the result.

Acknowledgments

This work is supported by Royal Society funding via A.Z.'s research project 'AMOS' RGS\R1\211053. Portions of this research were carried out at the ELI Beamlines Facility, a European user facility operated by the Extreme Light Infrastructure ERIC. The experiments were conducted at the HHG Beamline and we acknowledge the L1 & F-SYNC laser team. M.K. and R.J. acknowledges Royal Society funding under URF\R1\231460. Computer time for this study was provided by the computing facilities of the MCIA (Mésocentre de Calcul Intensif Aquitain) and King's Computational Research, Engineering and Technology Environment (CREATE) from King's College London.

Author contributions

A.Z. supervised and funded the project; O.H., L.J., O.F., M.A. contributed to the development and operation of the HHG beamline; L.J. designed the measurement setup for the MgO, including sample holders and motorization stages; C.Z., L.J., X.Z. performed the experiment under the guidance of A.Z. and O.H.; F.C. developed the algorithm and implemented the calculation code; C.Z. used F.C.'s code to simulate the experiment under the guidance of F.C.; C.Z. and L.J. did calibration of the experiment; C.Z., X.Z. analysed the data and prepared the figures; C.Z., A.Z., F.C., B.T.Q.M., R.M.J., M.K. wrote the manuscript with input from all authors. All authors participated in the discussions and interpretation of the data.

Competing interests

The authors declare no competing interests.

References

- [1] S. M. CAVALETTO et al. The attoscience of strong-field-driven solids. *Nature Reviews Physics* **7** no. 1, pp. 38–49 (2025).
- [2] C. HEIDE et al. Ultrafast high-harmonic spectroscopy of solids. *Nature Physics* **20** no. 10, pp. 1546–1557 (2024).
- [3] E. GOULIELMAKIS AND T. BRABEC. High harmonic generation in condensed matter. *Nature Photonics* **16** no. 6, pp. 411–421 (2022).
- [4] S. GHIMIRE AND D. A. REIS. High-harmonic generation from solids. *Nature Physics* **15** no. 1, pp. 10–16 (2019).
- [5] Z. TAO et al. Direct time-domain observation of attosecond final-state lifetimes in photoemission from solids. *Science* **353** no. 6294, pp. 62–67 (2016).
- [6] G. PITRUZZELLO. A bright future for attosecond physics. *Nature Photonics* **16** no. 8, pp. 550–552 (2022).
- [7] A. MCPHERSON et al. Studies of multiphoton production of vacuum-ultraviolet radiation in the rare gases. *Journal of the Optical Society of America B* **4** no. 4, pp. 595–601 (1987).
- [8] M. FERRAY et al. Multiple-harmonic conversion of 1064 nm radiation in rare gases. *Journal of Physics B: Atomic, Molecular and Optical Physics* **21** no. 3, p. L31 (1988).
- [9] A. RUNDQUIST et al. Phase-matched generation of coherent soft X-rays. *Science* **280** no. 5368, pp. 1412–1415 (1998).
- [10] P.-M. PAUL et al. Observation of a train of attosecond pulses from high harmonic generation. *Science* **292** no. 5522, pp. 1689–1692 (2001).
- [11] X. SHI et al. Attosecond light science and its application for probing quantum materials. *Journal of Physics B: Atomic, Molecular and Optical Physics* **53** no. 18, pp. 184 008–184 008 (2020).
- [12] M. HENTSCHEL et al. Attosecond metrology. *Nature* **414** no. 6863, pp. 509–513 (2001).
- [13] S. GHIMIRE et al. Observation of high-order harmonic generation in a bulk crystal. *Nature Physics* **7** no. 2, pp. 138–141 (2011).
- [14] O. SCHUBERT et al. Sub-cycle control of terahertz high-harmonic generation by dynamical bloch oscillations. *Nature Photonics* **8** no. 2, pp. 119–123 (2014).
- [15] J. PARK et al. Recent trends in high-order harmonic generation in solids. *Advances in Physics: X* **7** no. 1, p. 2003 244 (2022).
- [16] J. LI et al. Attosecond science based on high harmonic generation from gases and solids. *Nature Communications* **11** no. 1, p. 2748 (2020).
- [17] G. VAMPA et al. Semiclassical analysis of high harmonic generation in bulk crystals. *Physical Review B* **91** no. 6, p. 064 302 (2015).
- [18] G. VAMPA AND T. BRABEC. Merge of high harmonic generation from gases and solids and its implications for attosecond science. *Journal of Physics B: Atomic, Molecular and Optical Physics* **50** no. 8, p. 083 001 (2017).

- [19] G. VAMPA et al. All-optical reconstruction of crystal band structure. [*Physical Review Letters* **115** no. 19, p. 193 603 \(2015\).](#)
- [20] T. T. LUU et al. Extreme ultraviolet high-harmonic spectroscopy of solids. [*Nature* **521** no. 7553, pp. 498–502 \(2015\).](#)
- [21] F. CATOIRE et al. Wannier representation of intra-band high-order harmonic generation. [*Physical Review Letters* **121**, p. 143 902 \(2018\).](#)
- [22] M. WU et al. High-harmonic generation from bloch electrons in solids. [*Physical Review A* **91** no. 4, p. 043 839 \(2015\).](#)
- [23] M. WU et al. Multilevel perspective on high-order harmonic generation in solids. [*Physical Review A* **94** no. 6, p. 063 403 \(2016\).](#)
- [24] L. YUE et al. Signatures of multiband effects in high-harmonic generation in monolayer MoS₂. [*Physical Review Letters* **129** no. 14, p. 147 401 \(2022\).](#)
- [25] Á. JIMÉNEZ-GALÁN et al. Orbital perspective on high-harmonic generation from solids. [*Nature Communications* **14** no. 1, p. 8421 \(2023\).](#)
- [26] T. T. LUU AND H. J. WÖRNER. High-order harmonic generation in solids: A unifying approach. [*Physical Review B* **94** no. 11, p. 115 164 \(2016\).](#)
- [27] A. A. LANIN et al. High-order harmonic analysis of anisotropic petahertz photocurrents in solids. [*Optics Letters* **44** no. 8, pp. 1888–1891 \(2019\).](#)
- [28] O. NEUFELD, D. PODOLSKY AND O. COHEN. Floquet group theory and its application to selection rules in harmonic generation. [*Nature communications* **10** no. 1, p. 405 \(2019\).](#)
- [29] Y. S. YOU et al. Laser waveform control of extreme ultraviolet high harmonics from solids. [*Optics Letters* **42** no. 9, pp. 1816–1819 \(2017\).](#)
- [30] T. T. LUU AND H. J. WÖRNER. Measurement of the Berry curvature of solids using high-harmonic spectroscopy. [*Nature Communications* **9** no. 1, p. 916 \(2018\).](#)
- [31] A. J. UZAN-NAROVLSKY et al. Observation of inter-band Berry phase in laser-driven crystals. [*Nature* **626** no. 7997, pp. 66–71 \(2024\).](#)
- [32] D. BAYKUSHEVA et al. All-optical probe of three-dimensional topological insulators based on high-harmonic generation by circularly polarized laser fields. [*Nano Letters* **21** no. 21, pp. 8970–8978 \(2021\).](#)
- [33] D. BAYKUSHEVA et al. Strong-field physics in three-dimensional topological insulators. [*Physical Review A* **103** no. 2, p. 023 101 \(2021\).](#)
- [34] R. SILVA et al. High-harmonic spectroscopy of ultrafast many-body dynamics in strongly correlated systems. [*Nature Photonics* **12** no. 5, pp. 266–270 \(2018\).](#)
- [35] Y. BAI et al. High-harmonic generation from topological surface states. [*Nature Physics* **17** no. 3, pp. 311–315 \(2021\).](#)
- [36] F. BLOCH. Über die quantenmechanik der elektronen in kristallgittern. [*Zeitschrift für physik* **52** no. 7, pp. 555–600 \(1929\).](#)
- [37] N. H. LINDNER, G. REFAEL AND V. GALITSKI. Floquet topological insulator in semiconductor quantum wells. [*Nature Physics* **7** no. 6, pp. 490–495 \(2011\).](#)
- [38] M. C. RECHTSMAN et al. Photonic Floquet topological insulators. [*Nature* **496** no. 7444, pp. 196–200 \(2013\).](#)
- [39] H. WANG, L. ZHOU AND Y. D. CHONG. Floquet Weyl phases in a three-dimensional network model. [*Physical Review B* **93** no. 14, p. 144 114 \(2016\).](#)
- [40] P. TITUM et al. Disorder-induced Floquet topological insulators. [*Physical Review Letters* **114** no. 5, p. 056 801 \(2015\).](#)
- [41] H. LIGNIER et al. Dynamical control of matter-wave tunneling in periodic potentials. [*Physical Review Letters* **99** no. 22, p. 220 403 \(2007\).](#)
- [42] J. H. SHIRLEY. Solution of the Schrödinger equation with a Hamiltonian periodic in time. [*Physical Review* **138** no. 4B, p. B979 \(1965\).](#)
- [43] H. SAMBE. Steady states and quasienergies of a quantum-mechanical system in an oscillating field. [*Physical Review A* **7** no. 6, p. 2203 \(1973\).](#)
- [44] F. FAISAL AND R. GENIESER. Exact solution of the kronig-penney model of 1d crystals in strong laser fields. [*Physics Letters A* **141** no. 5–6, pp. 297–300 \(1989\).](#)
- [45] M. GRIFONI AND P. HÄNGGI. Driven quantum tunneling. [*Physics Reports* **304** no. 5–6, pp. 229–354 \(1998\).](#)
- [46] S. ITO et al. Build-up and dephasing of Floquet-Bloch bands on subcycle timescales. [*Nature* **616** no. 7958, pp. 696–701 \(2023\).](#)
- [47] Y. WANG et al. Observation of Floquet-Bloch states on the surface of a topological insulator. [*Science* **342** no. 6157, pp. 453–457 \(2013\).](#)
- [48] J.-Z. JIN et al. Contribution of Floquet-Bloch states to high-order harmonic generation in solids. [*Physical Review A* **100** no. 1, p. 013 412 \(2019\).](#)
- [49] T. N. IKEDA, K. CHINZEI AND H. TSUNETSUGU. Floquet-theoretical formulation and analysis of high-order harmonic generation in solids. [*Physical Review A* **98** no. 6, p. 063 426 \(2018\).](#)
- [50] H. YAMANE AND S. TANAKA. Ultrafast dynamics of high-harmonic generation in terms of complex floquet spectral analysis. [*Symmetry* **10** no. 8, p. 313 \(2018\).](#)
- [51] F. CATOIRE AND H. BACHAU. Above-threshold ionization of quasiperiodic structures by low-frequency laser fields. [*Physical Review Letters* **115** no. 16, p. 163 602 \(2015\).](#)
- [52] P. STAMMER. On the limitations of the semi-classical picture in high harmonic generation. [*Nature Physics* **20** no. 7, pp. 1040–1042 \(2024\).](#)
- [53] C. HEIDE et al. Ultrafast high-harmonic spectroscopy of solids. [*Nature Physics* **20**, pp. 1546–1557 \(2024\).](#)
- [54] V. CHANG LEE et al. Many-body enhancement of high-harmonic generation in monolayer MoS₂. [*Nature Communications* **15** no. 1, p. 6228 \(2024\).](#)
- [55] A. J. UZAN-NAROVLSKY et al. Observation of light-driven band structure via multiband high-harmonic spectroscopy. [*Nature Photonics* **16** no. 6, pp. 428–432 \(2022\).](#)
- [56] F. FAISAL AND J. KAMIŃSKI. Floquet-Bloch theory of high-harmonic generation in periodic structures. [*Physical Review A* **56** no. 1, p. 748 \(1997\).](#)
- [57] V. STRELKOV. Role of autoionizing state in resonant high-order harmonic generation and attosecond pulse production. [*Phys. Rev. Lett.* **104**, p. 123 901 \(2010\).](#)

- [58] H. ALLEGRE et al. Extension of high-harmonic generation cutoff in solids to 50 eV using MgO. [Optics Letters](#) **50** no. 5, pp. 1492–1495 (2025).
- [59] M. G. MEDVEDEV et al. Density functional theory is straying from the path toward the exact functional. [Science](#) **355** no. 6320, pp. 49–52 (2017).
- [60] M. A. MARQUES et al. octopus: a first-principles tool for excited electron-ion dynamics. [Computer Physics Communications](#) **151** no. 1, pp. 60–78 (2003).
- [61] A. CASTRO et al. Octopus: a tool for the application of time-dependent density functional theory. [Physica Status Solidi \(b\)](#) **243** no. 11, pp. 2465–2488 (2006).
- [62] W. KOHN AND L. J. SHAM. Self-consistent equations including exchange and correlation effects. [Physical Review](#) **140** no. 4A, p. A1133 (1965).
- [63] D. R. HAMANN. Optimized norm-conserving vanderbilt pseudopotentials. [Physical Review B](#) **88**, p. 085 117 (2013).
- [64] M. SCHLIPF AND F. GYGI. Optimization algorithm for the generation of oncv pseudopotentials. [Computer Physics Communications](#) **196**, p. 36 (2015).
- [65] P. SCHERPELZ et al. Implementation and validation of fully relativistic gw calculations: Spin–orbit coupling in molecules, nanocrystals, and solids. [Journal of Chemical Theory and Computation](#) **12**, p. 3523 (2016).
- [66] J. VÁBEK, H. BACHAU AND F. CATOIRE. Ionization dynamics and gauge invariance. [Physical Review A](#) **106** no. 5, p. 053 115 (2022).